RISING BUBBLE IN A VERTICAL SLOWLY DIVERGING PIPE

Gustavo Anjos*

GESAR, Universidade do Estado do Rio de Janeiro, Brazil

*gustavo.anjos@uerj.br

Erik Gros

LTCM, École Polytechnique Fédérale de Lausanne, Switzerland

Kamal Selvam & Jorge Peixinho

LOMC, CNRS & Université Le Havre Normandie, France

Abstract. We present the results of a combined experimental and numerical study of an air bubble rising in a vertical slowly diverging pipe in a stagnant liquid. Initially, the bubble is confined in a cylindrical tube and rises due to buoyancy in the same manner as a Taylor or elongated bubble. When the bubble moves upwards, it reduces its vertical height and the shape of the bubble transitions to a spherical cap bubble. Different tests with various liquids are reported and a numerical simulation using two-dimensional axisymmetric finite element method for two-phase flow is reported. An adaptative mesh is also used to compute the bubble dynamics. The experimental and the simulation results are compared in terms of rising velocity and bubble aspect ratio. Our results show a puzzling feature that is the bubble dynamics and topology strongly depends on the initial conditions.

Keywords: rising bubble, instability, interface, diverging pipe

1. INTRODUCTION

Large bubbles in tubes are known to exhibit rich interfacial dynamics (e.g. see textbooks by Clift *et al.* (1978) and de Gennes *et al.* (2002)), but their motions in slowly diverging tubes have not been examined although such geometry can be encountered in industrial or physiologic applications. This geometry is of fundamental interest because flow in a divergent tubes can be seen as a simple example of multi-scale system. Indeed, in a numerical work, the grid would have to adapt the refinement along the flow as the diameter of the pipe increases. However, interfacial tracking methods usually require constant element size in order to capture the interface dynamics accurately. This type of problem constitutes a simple test problem for adaptive mesh methods.

A motivation behind the study of the rising of a bubble in a slowly diverging tube is the search for the transition between different types of bubbles usually only achievable in numerical works; e.g. Bonometti and Magnaudet (2006) looked at the transition between a spherical cap bubble and toroidal bubble. Specifically here, we study the transition from a confined large bubble, often called Taylor bubble in reference to the landmark paper by Davies and Taylor (1950), to an unconfined bubble or a spherical cap bubble, see e.g. Wegener and Parlange (1973). This transition from Taylor bubble (elongated bubble) to spherical cap bubble can be seen as a simple case of slug-bubbly flow transition.

Taylor bubbles in straight tubes have been extensively studied and their propagation régimes are well documented (e.g. see Davies and Taylor (1950), Bretherton (1961), Zukoski (1966), Viana *et al.* (2003), Funada *et al.* (2005) and others). Recently, the propagation régimes for the motion of bubble in channels of arbitrary cross-sections by Clanet *et al.* (2004) and de Lózar *et al.* (2007) and curved channels by Muradoglu and Stone (2007) have been reported. One feature of the Taylor bubble is its stable axisymmetric shape and surrounding flow field. The dependence of the bubble rising velocity under an inclined planed was reported by Assillous and Quéré (2002). This experiments showed that dependence of the rising velocity upon the initial bubble volume and the importance of the liquid film between the bubble and the wall. The stability of this flow has been also addressed in several studies by Batchelor (1987), Levine and Yang (1990), Lu and Prosperetti (2006) and others. Batchelor argued that the stabilisation mechanism depends on the convection over the bubble i.e. disturbances are transported along the bubble surface. By comparing the growth rate of disturbance and the bubble radius, Batchelor (1987) gave some criteria for the break-up of bubble. Also, spatial and temporal growth rates of the disturbances are fundamental understand this stability problem.

During the last decades, computational techniques capable of dealing with free-surface flows in the presence of viscous effects and topological changes have been developed, for example the Volume of Fluid method, or VOF Hirt and Nichols (1981), which describes the position of the interface by the volume ratio occupied by each phase in the computational cells. Other methods like the Arbitrary Lagrangian-Eulerian Finite Element Method (ALE-FEM) have become available (Anjos, 2012; Anjos *et al.*, 2014). Although, it is possible to solve three-dimensional problems, it is sometimes useful and faster to consider two-dimensional solutions and axisymmetric solutions. Axisymmetric analytical solutions are sometimes available and relatively fast to compute.

Here, we describe the motion of relatively large bubble rising in stagnant liquid in a vertical diverging cylindrical tubes. The experimental set-up is presented in §2 prior the numerical setup in §3. Experimental and numerical results

for the position, velocity, aspect ratio of the rising bubble along the vertical position in §4, as well as the capillary wave properties that arise during rising. Finally, the conclusions of your study are presented in §5.

2. EXPERIMENTAL SETUP

The experiment consists of vertical diverging acrylic tube. The inlet diameter is 2.14 mm and the top diameter is 21.4 mm. The total length of the tube is 300 mm. Air is injected using a manual syringe or a syringe pump in a quasi-static manner from the bottom in a quiescent liquid at a flow rate Q. The tube is closed at the top. The bubble grows in the straight section below the slowly diverging tube. There is a liquid film between the air bubble and the tube wall.

Several liquids were used: de-ionised water (DW), mixtures of water and glycerol (DW+G) and several silicone oils (SO or HMDSO) with viscosity of 0.536 and 970 mPa.s. In these experiments, the Reynolds number $Re = \rho U_b D/\mu$ ranged from 10 to 10^4, where ρ is the liquid density, U_b is the bubble velocity, D is the diameter of the tube and μ is the liquid viscosity. The capillary length is defined as $a \equiv \sqrt{\gamma/(\rho g)}$ where γ is the surface tension, g is the gravity constant. Details on the fluid properties are given in the Results section in Table (2).

The bubble is formed by the injection of air in a straight pipe section below the diverging section. Air bubbles grow and move into the diverging section due to buoyancy forces. The bubble size is limited by a capillary instability of the liquid film similar to that reported in Duclaux *et al.* (2006). Observations were made in the direction orthogonal to the flow using a high speed camera and image analysis MATLAB programs.

Photographs of the bubble injection and shape evolution for different air injection rate can be found in Fig. 1a-d. The bubble aspect ratio, χ, is plotted as a function of height from the diverging section, L_d, in figure 1e. The results are presented for several bubbles.
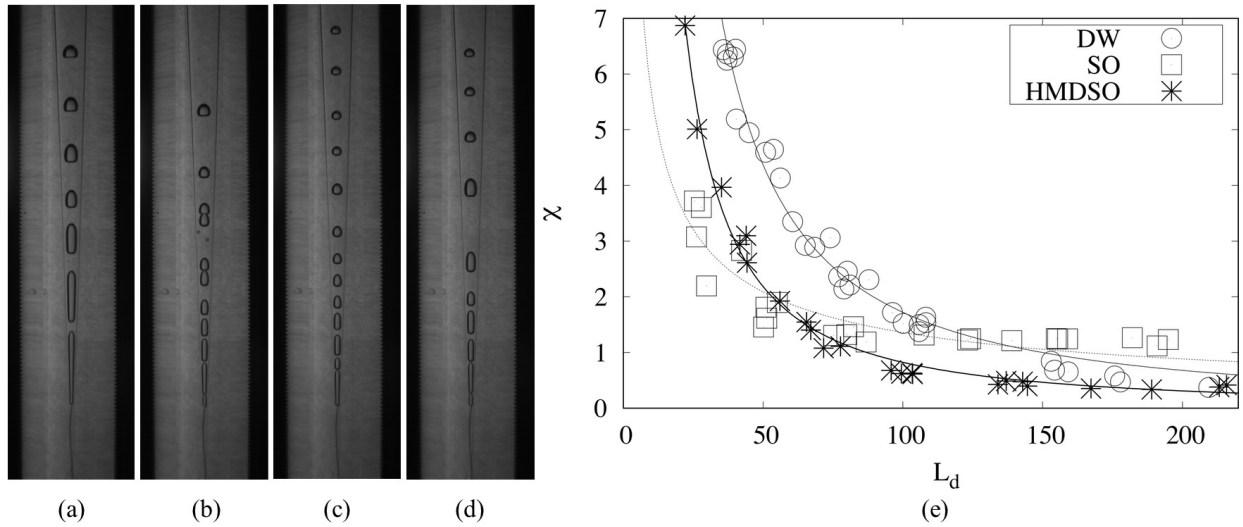

Figure 1: Experimental results for SO in the 4° divergent pipe. Photographs of a rising bubble at different positions along the tube (a) $Q = 2\ ml/min$, (b) 7.5, (c) 10, (d) 10 and (e) Evolution of the bubble aspect ratio, χ, as a function of the axial position, L_d, from the diverging section.

3. NUMERICAL SETUP

3.1 Governing Equations

We present the non-dimensional incompressible Navier-Stokes equations in cylindrical coordinates for axisymmetric flows, where the assumption of no tangential velocity is made. It is important noting that the strain tensor is here fully represented with components $\nabla \mathbf{v}$ and $(\nabla \mathbf{v})^T$ as follows:

$$\rho(x)\frac{D\mathbf{v}}{Dt} = -\nabla p + \frac{1}{N^{1/2}}\mu(x)\begin{bmatrix} 2\frac{1}{r}\frac{\partial}{\partial r}r\frac{\partial}{\partial r}v + \frac{\partial}{\partial x}\frac{\partial u}{\partial r} + \frac{\partial^2 v}{\partial^2 r} - \frac{2u}{r} \\ \frac{1}{r}\frac{\partial}{\partial r}r\frac{\partial}{\partial r}u + \frac{1}{r}\frac{\partial}{\partial r}r\frac{\partial}{\partial x}v + 2\frac{\partial^2 u}{\partial^2 x} \end{bmatrix} + \rho(x)\mathbf{g} + \frac{1}{Eo}\mathbf{f_{st}} \tag{1}$$

$$\frac{\partial u}{\partial x} + \frac{\partial v}{\partial r} + \frac{v}{r} = 0 \tag{2}$$

where $\rho(x)$ and $\mu(x)$ stand for the density and viscosity of the fluids in the numerical domain as a function of the position occupied by the fluid, $\mathbf{v}$ is the velocity field in axisymmetric coordinates with axial u and radial v components, t represents

time, p pressure, $\mathbf{g}$ is gravity and $\mathbf{f_{st}}$ represents the surface tension force according to Brackbill and Kothe (1992) and modeled as:

$$\mathbf{f_{st}} = \kappa \nabla H \tag{3}$$

where κ stand for curvature and ∇H is the gradient of the Heaviside function H, which is equal to one in the inner phase and zero in the outer phase. The non-dimensional numbers Archimedes N and Eötvös Eo are both defined as:

$$N = \frac{\rho_0^2 g_0 D^3}{\mu_0^2} \qquad\qquad Eo = \frac{\rho_0 g_0 D^2}{\sigma_0}$$

note that the above non-dimensional groups are achieved by using the standard parameters when the velocity of the system is unknown, thus replacing the common non-dimensionalization $u^* = u/U_0$ by $\mathbf{u}^* = \mathbf{u}/\sqrt{g_0 D_0}$ and $\mathbf{x}^* = \mathbf{x}/L$ by $\mathbf{x}^* = \mathbf{x}/D$, where U_0, L and D are referential parameters of velocity, length and tube diameter respectively and $*$ stands for the non-dimensional quantities. Additionally, the non-dimensional Morton number and Capillary number are defined due to their importance to characterize the shape of a bubble or (drop) and the relative effect of the viscous and surface tension forces, respectively:

$$Mo = \frac{\mu_0^4 g_0}{\rho_0 \sigma_0^3} = Eo^3 N^2 \qquad\qquad Ca = \frac{\mu_0 U_0}{\sigma_0}$$

The material derivative $D\mathbf{v}/Dt$ is defined in the Arbitrary Eulerian-Lagrangian framework as follows:

$$\frac{D\mathbf{v}}{Dt} = \frac{\partial \mathbf{v}}{\partial t} + \mathbf{c} \cdot \nabla \mathbf{v} \tag{4}$$

where $\mathbf{c}$ represents the difference between the fluid flow $\mathbf{v}$ and the mesh velocity $\hat{\mathbf{v}}$. If the mesh velocity $\hat{\mathbf{v}} = 0$, the *Eulerian* framework is achieved, on the other hand if $\hat{\mathbf{v}} = \mathbf{v}$, the *Lagrangian* framework is achieved. The gradient in axisymmetric formulation read as $\nabla \bullet = (\partial \bullet /\partial x, \partial \bullet /\partial r)^T$.

Boundary conditions are required to find the particular solution of the partial differential equations presented above for the solution of the two-phase flow system. Since the geometry and the flow variables are assumed to be independent of the rotation angle θ, a symmetry boundary condition of

$$v = 0 \qquad \text{and} \qquad \frac{\partial u}{\partial r} = 0 \tag{5}$$

is required on the symmetry axis ($r = 0$). Since the flow of the present study is driven by gravitational effects, the *no-slip* condition is used at all the remaining walls except the exit wall where pressure is set to a reference value.

3.2 Variational Formulation

Let us consider the space $H1(\Omega)$ as being the space of functions in $L_1^2(\Omega)$ such that their first partial derivatives are also in $L_1^2(\Omega)$. The spaces $\mathfrak{U}_{u_D}$, $\mathfrak{V}_{v_D}$ are defined as:

$$\mathfrak{U}_{u_D} := \{u \in H_1^1(\Omega)|u = u_D \quad \text{on} \quad \Gamma_D\}, \tag{6}$$

$$\mathfrak{V}_{v_D} := \{v \in H_1^1(\Omega)|v \in L_{-1}^2 \quad \text{and} \quad v = v_D \quad \text{on} \quad \Gamma_D\} \tag{7}$$

The weak form of the Navier-Stokes equations: find $(v, p) \in \mathfrak{U}_{u_D} \times \mathfrak{V}_{v_D} \times \mathfrak{Q}$ such that:

$$M_\rho \left(\frac{D\mathbf{v}}{Dt}, \mathbf{w}\right) + \frac{1}{Re} K(\mathbf{v}, \mathbf{w} = M(\mathbf{g}, \mathbf{w}) + \frac{1}{We} G(H, k\mathbf{w}) \tag{8}$$

$$D(q, \mathbf{v}) = 0 \tag{9}$$

for all $(\mathbf{w}, q) \in \mathfrak{U}_0 \times \mathfrak{V}_0 \times \mathfrak{Q}$. Here, M, K, G and D are the mass, stiffness, gradient and divergent matrices respectivelly, and $d\mathbf{x} = dr\,dx$. The bilinear forms are therefore defined as follows:

$$M(\mathbf{v}, \mathbf{w}) = \int_{\Omega} \mathbf{w} \cdot \mathbf{v} \, r d\mathbf{x} \qquad\qquad M_{\rho}(\mathbf{v}, \mathbf{w}) = \int_{\Omega} \rho(x) \mathbf{w} \cdot \mathbf{v} \, r d\mathbf{x}$$

$$K(\mathbf{v}, \mathbf{w}) = 2 \int_{\Omega} \mu(x) \mathcal{D}(\mathbf{w}) : \mathcal{D}(\mathbf{v}) \, r d\mathbf{x} + \int_{\Omega} \mu \frac{w_2 v}{r^2} \, r d\mathbf{x} \qquad\qquad (10)$$

$$G(p, \mathbf{w}) = \int_{\Omega} \mathbf{w} \cdot \nabla p \, r d\mathbf{x} \qquad\qquad D(\mathbf{v}, q) = \int_{\Omega} q \nabla \cdot \mathbf{v} \, r d\mathbf{x}$$

where $2\mathcal{D}(\mathbf{v}) = \nabla \mathbf{v} + (\nabla \mathbf{v})^T$.

3.3 Assembling

We shall define the local element matrices m, m_{ρ}, k_{xx}, k_{rx}, k_{xr}, k_{rr}, km_{rr}, g_x, g_r, d_x, d_r and dm_r as follows:

$$m_{x,ij}^e = m_{r,ij}^e = \int_{\Omega^e} N_i^e N_j^e \, r \, d\mathbf{x} \qquad\qquad m_{\rho,x,ij}^e = m_{\rho,r,ij}^e = \int_{\Omega^e} \rho^e N_i^e N_j^e \, r \, d\mathbf{x}$$

$$k_{xx,ij}^e = \int_{\Omega^e} \mu^e \left(\frac{\partial N_i^e}{\partial x} \frac{\partial N_j^e}{\partial x} \right) r \, d\mathbf{x} \qquad\qquad k_{xr,ij}^e = \int_{\Omega^e} \mu^e \left(\frac{\partial N_i^e}{\partial r} \frac{\partial N_j^e}{\partial x} \right) r \, d\mathbf{x}$$

$$k_{rx,ij}^e = \int_{\Omega^e} \mu^e \left(\frac{\partial N_i^e}{\partial x} \frac{\partial N_j^e}{\partial r} \right) r \, d\mathbf{x} \qquad\qquad k_{rr,ij}^e = \int_{\Omega^e} \mu^e \left(\frac{\partial N_i^e}{\partial y} \frac{\partial N_j^e}{\partial y} \right) r \, d\mathbf{x}$$

$$km_{rr,ij}^e = \int_{\Omega^e} \frac{\mu^e}{r^2} (N_i^e N_j^e) \, r \, d\mathbf{x} \qquad\qquad g_{x,ik}^e = \int_{\Omega^e} N_i^e \frac{\partial Q_k^e}{\partial x} \, r \, d\mathbf{x}$$

$$g_{r,ik}^e = \int_{\Omega^e} N_i^e \frac{\partial Q_k^e}{\partial r} \, r \, d\mathbf{x} \qquad\qquad d_{x,kj}^e = \int_{\Omega^e} Q_k^e \frac{\partial N_j^e}{\partial x} \, r \, d\mathbf{x}$$

$$d_{r,kj}^e = \int_{\Omega^e} Q_k^e \frac{\partial N_j^e}{\partial r} \, r \, d\mathbf{x} \qquad\qquad dm_{r,kj}^e = \int_{\Omega^e} Q_k^e N_j^e \, r \, d\mathbf{x}$$

Note here that the fluid properties ρ and μ are taken to be constant in the element, thus achieving a sharp transition between phases. The assembling procedure will produce the matrices M, M_{ρ}, K, G and D, defined as:

$$\mathbf{M} = \left[\begin{array}{cc} M_x & 0 \\ 0 & M_r \end{array} \right]_{2NV \times 2NV} \mathbf{M}_{\rho} = \left[\begin{array}{cc} M_{\rho,x} & 0 \\ 0 & M_{\rho,r} \end{array} \right]_{2NV \times 2NV}$$

$$\mathbf{K} = \left[\begin{array}{cc} 2K_{xx} + K_{rr} & K_{rx} \\ K_{xr} & K_{xx} + 2K_{rr} + 2KM_{rr} \end{array} \right]_{2NV \times 2NV} \mathbf{G} = \left[\begin{array}{c} G_x \\ G_r \end{array} \right]_{2NV \times NP}$$

$$\mathbf{D} = \left[\begin{array}{cc} D_x & D_r + DM_r \end{array} \right]_{NP \times 2NV}$$

here, NV are the total number of unknowns of velocity and NP is the total number of unknowns for pressure. The matrices presented above represent the discretization of the differential operators and the system mass that will produce the final linear system for the solution of the velocity field $\mathbf{v}$ and pressure p.

3.4 Adaptive dynamic refinement

Two-Phase flows in ALE context requires the interface between fluids to be moved with the flow velocity, therefore the constant motion of the interface must be handled efficiently to avoid large finite element distortion and, consequently, lack of accuracy to compute the operators. Moreover, the motion of the interface can lead to large mesh density in unwanted regions and lack of elements in others. If flow occurs in the neighborhood of the interface, the domain mesh can also suffer of severe deformation, thus leading to the interruption of the simulation. To remedy such a potential damage in both the interface and the domain meshes, an adaptive moving mesh refinement must be present. In this axisymmetric in-house code, we have implemented a flexible and efficient way to handle small to large mesh distortions using a combination of robust and modern algorithms such as the well known Laplacian smooth operator, as well as, the capability of insert and delete nodes during the simulation. All the incorporated techniques can be easily accessed by parameters passed to the simulator, which can be constant or variable if required by a certain condition. It is important to highlight that a smart node distribution has been implemented to set mesh density in different regions of the domain. Such a node distribution is achieved by the solution of the Helmholtz equation for the unknown edge length h. Moreover, a Delaunay triangulation

algorithm ensures an optimal node connectives based on geometry properties. Such an algorithm was incorporated in the in-house code as an external library Shewchuk (1997) and has not been developed by our group. All remeshing techniques available can be found in details in Anjos (2012).

3.5 Numerical Model

We proposed two inf-sup stable finite-element pairs for the discretization of the equations in the numerical domain: the mini element (P_1^{bubble}; P_1) and the quadratic+bubble element (P_2^{bubble}; P_1). The former being continuous piecewise linear polynomials enriched by a cubic bubble function for the velocity components and continuous piecewise linear for the pressure, whilst the latter is continuous piecewise quadratic polynomials enriched by a cubic bubble function for the velocity components and continuous piecewise linear for the pressure as can be seen in Fig. (2).
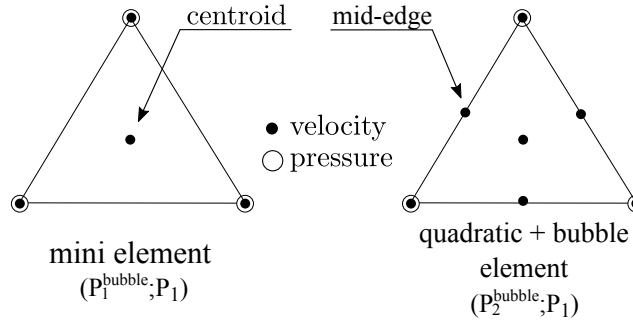

Figure 2: Interpolation nodes for inf-sup stable finite-element pairs: the mini element and the quadratic+bubble element.

In the current method, discretization of the non-linear convective term is avoided by discretizing the material derivative. This approach is referred to the semi-Lagrangian since the Lagrangian description of motion is used for the left hand side of Eq. (1) while its right hand side is expressed in the usual Eulerian form. The semi-Lagrangian algorithm is an integrating factor method in which such a factor is an advection operator. This operator is shifted to a moving coordinate system from which the next time step quantity is calculated. The Semi-Lagrangian of the velocity field may be discretized linearly in the time domain at the point xi by using a explicit first order scheme:

$$\frac{D\mathbf{v}}{Dt} \approx \frac{\mathbf{v_i}^{n+1}(\mathbf{x}) - \mathbf{v}_d^i(\mathbf{x}_d)}{\Delta t} \tag{11}$$

where $\mathbf{v}^n(\mathbf{x}) = \mathbf{v}(\mathbf{x}, t^n)$ and $\mathbf{x}_d$ is the departure point of the fluid particle at position x. The departure position is found by integrating the velocity backwards in time assuming the velocity to be constant and equal to the velocity at the previous time step:

$$\mathbf{x}^d = \mathbf{x} - (t^{n+1} - t^n)\mathbf{v}^n(\mathbf{x}) \tag{12}$$

After time discretization, the following fully discrete system may be obtained: find $(\mathbf{v}^{n+1}, p^{n+1}) \in \mathfrak{U}_{u_D} \times \mathfrak{V}_{v_D} \times \mathfrak{Q}$ such that:

$$\frac{M_\rho}{\Delta t}\mathbf{v}^{n+1} + \frac{1}{Re}K\mathbf{v}^{n+1} + Gp^{n+1} = \frac{M_\rho}{\Delta t}\mathbf{v}(\mathbf{x}_d)^n + M_\rho\mathbf{g} + \frac{M}{Eo}\mathbf{f_{st}} \tag{13}$$

$$D\mathbf{v}^{n+1} = 0 \tag{14}$$

In the present work, the solution of the final linear systems are solved uncoupled, i.e. using the projection method based on the LU decomposition to uncouple velocity and pressure, at each time step by a direct solver, based on LU factorization, as a preconditioner using the external library PETSc (Balay *et al.* (2011b,a)). Note that the time step used in all simulations had the restriction of the smaller time step of all explicitly treated terms, where for the simulations presented in this work, the time step restriction given by the surface tension was the larger.

4. RESULTS

In this section, a challenging test has been carried out to validate the code against the terminal velocity, film thickness and the shape of elongated air bubbles in circular channels. The wall effects are included in the bubble dynamics and the

Table 1: Fluid properties for the rising of air Taylor bubble

fluid	properties			dimensionless number		film thickness
	ρ $[kg/m^3]$	μ $[\mu Pa \cdot s]$	σ $[mN/m]$	Eo [-]	Mo [-]	δ [-]
sucrose	1.172	5.650	77.7	40	1E-07	0.0617
glycerol	1.260	712.0	63.1	40	1E-01	0.1483
diluted glycerol	0.234	154.0	64.8	100	1E-02	0.1196
air	1.789	1.225	—	—	—	—

results are compared to the well known flow pattern map of White and Beardmore (1962), the Brown's theoretical solution for the film thickness Brown (1965) and to the 3-dimensional code developed by Anjos (2012); Anjos *et al.* (2014) using the same methodology. The modeling of such flows increases significantly the obstacles of the remeshing process, since the formation of the thin liquid film between the bubble and wall requires a fine mesh to capture the flow mechanisms. Again, the flexibility of the Finite Element method is explored in the development of the computational meshes, in which different mesh element sizes are used in this axisymmetric domain. Next, we presented results of the axisymmetric model proposed here to simulate the rising of elongated bubble in a vertical slowly diverging pipe, where transition of elongated to spherical cap bubble shape has been investigated.

4.1 Validation: Rising of Taylor air bubble

To characterize the rising velocity of air bubbles in different solutions, we identified 3 regions in the flow pattern map for the numerical simulations. Two solutions of glycerol and one of sucrose has been used. Table 1 summarizes the fluid properties used in the rising Taylor (elongated) bubble simulations. The $(P_2^{bubble}; P_1)$ (quad + bubble element) has been used at all simulations of the rising of Taylor air bubble.

The numerical solution for the rising bubble requires a long domain to be compatible to the experiments. According to Bugg *et al.* (1998), the development of the bubble's shape and, consequently, the terminal velocity requires that the numerical domain should be $8D$ long in the gravity direction. As mentioned before, an extra mesh refinement is needed to solve the liquid film formed between the wall and the confined bubble, thus the total number of mesh elements increases dramatically. Considering that the simulations are performed in 3-dimensions and the experimental test section is constant in the gravity direction, a moving referential frame technique is employed to shorten the numerical domain, thus allowing a faster computation.

The numerical domain used to simulate all the fluids given by Table (1) was set to $D \times 5D + L_b$, where D stands for the circular channel diameter and L_b is the bubble length. The bubble was placed far from the bottom part of the domain to guarantee that the bubble's wake is well captured, thus allowing the bottom of the bubble to deform.

Figure (3) shows the time progression of a Taylor air bubble immersed in a sucrose solution. The same bubble shape and film thickness, as the previous cases, is used as an initial shape. In the transient evolution, the bubble's velocity reached its maximum velocity at time $t \approx 1$, and its terminal velocity at time $t \approx 3.7$ Also, it was shown that the bottom part of the bubble was pulled in and oscillated until convergence at $t \approx 7.4$ The mesh parameters used in this simulation were $\beta_1 = 0.0$, $\beta_2 = 1.0$, $\gamma_1 = 1.0$ and $\gamma_2 = 0.1$ and the dimensionless numbers were set to $Mo = 1e - 7$, $Eo = 40$. Figure (4 presents the transient solution of the bubble's center of mass velocity. It was observed, an overshooting of the ascension velocity from time $t = 0$ to $t = 1.1$, due to the initial deformation of the bottom part of the bubble, and consequently acceleration of the center of mass. The result agreed to the prediction of the flow pattern map, obtaining an error of 1.1%.

Figure (5) show the evolution in time of the bubble's center of mass velocity, in which the computed terminal velocity approaches the value found in the flow pattern map. The error was found to be 6.5%. The mesh parameters used in this simulation were $\beta_1 = 0.0$, $\beta_2 = 0.5$, $\gamma_1 = 0.5$ and $\gamma_2 = 0.1$ and the pair of dimensionless numbers was set to $Mo = 1e - 2$, $Eo = 100$ and $Mo = 1e - 1$, $Eo = 40$. In this case, the mesh parameters were slightly modified to test different mesh conditions in the simulation. The obtained result shows that the bubble shape and terminal velocity agrees well to experimental data.

At our simulations, the film thickness of the rising of the Taylor bubbles presented errors of $4 - 6\%$ compared to the correlation of Brown (1965). It is important to note that the liquid film for the Taylor bubble simulations adds significantly the difficult of handling the mesh in the liquid film. However, with the proposed adaptive mesh refinement, the dynamics of the bubble rise could be essentially captured.

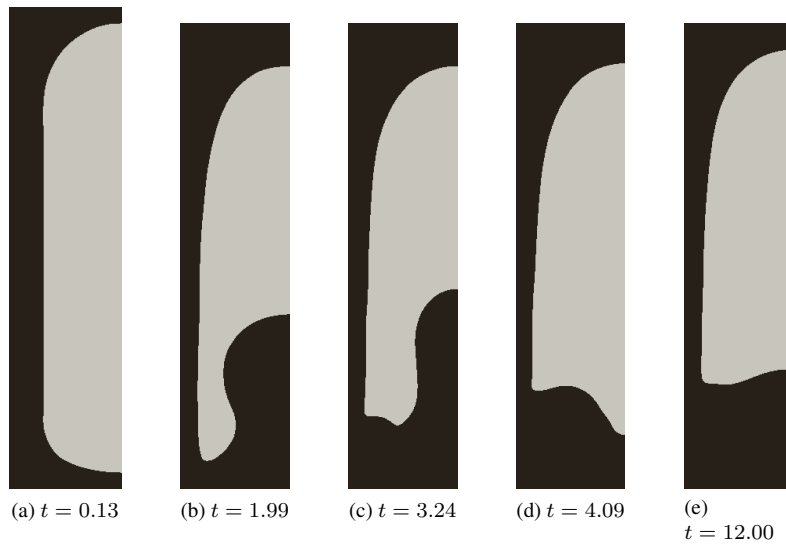(a) $t = 0.13$ (b) $t = 1.99$ (c) $t = 3.24$ (d) $t = 4.09$ (e) $t = 12.00$

Figure 3: Bubble shape evolution with time for an air bubble in a sucrose solution with dimensionless numbers $Mo = 1e - 7$, $Eo = 40$. The adaptive mesh refinement proposed in this work captures accurately the strong shape distortion produced by the high ascension velocity. (a) Initial bubble shape with $t = 0.13$. (b-d) Bubble shape change during transient solution. (e) Terminal bubble shape with $t = 12.00$.
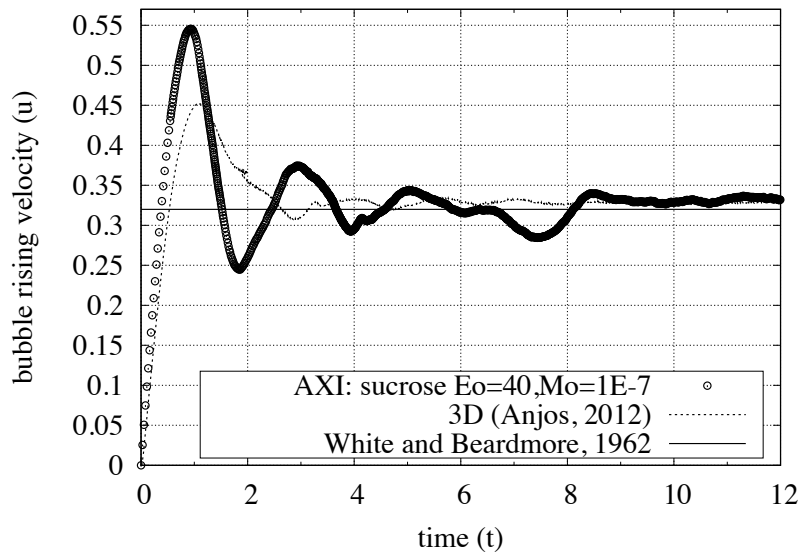

Figure 4: Rising of an air Taylor bubble immersed in a sucrose solution with dimensionless numbers set to $Mo = 1e - 7$ and $Eo = 40$. The time evolution of the Bubble's center of mass velocity is compared to the terminal bubble's velocity found in White and Beardmore (1962). Velocity and time are non-dimensional.

4.2 Comparison: Divergent pipe

We simulated numerically three fluids namely de-ionised water (DW), mixtures of water and glycerol (DW+G) and silicone oil (HMDSO) using dimensionless equations and geometry. The numerical solution for the rising bubble in divergent pipe requires a large domain to be compatible to the experiments, and for numerical purpose we shortened the non-dimensional pipe length to $L = 60D$, which represents a total dimension of 126 mm. This procedure is justified by the interesting of the numerical investigation in the initial divergent section where transition from elongated to spherical cap bubble occurs. The bubble was placed far from the bottom part of the domain to guarantee that the bubble's wake is well captured. A detailed description of the geometry and initial configuration used can be seen in Fig. (6). The fluid properties used to simulate all the fluids in given in Table (2). The $(P_1^{bubble}; P_1)$ (mini-element) has been used at all simulations of the divergent pipe.

The remeshing strategy was applied to all simulations successfully and it has shown to be consistent and robust. It is
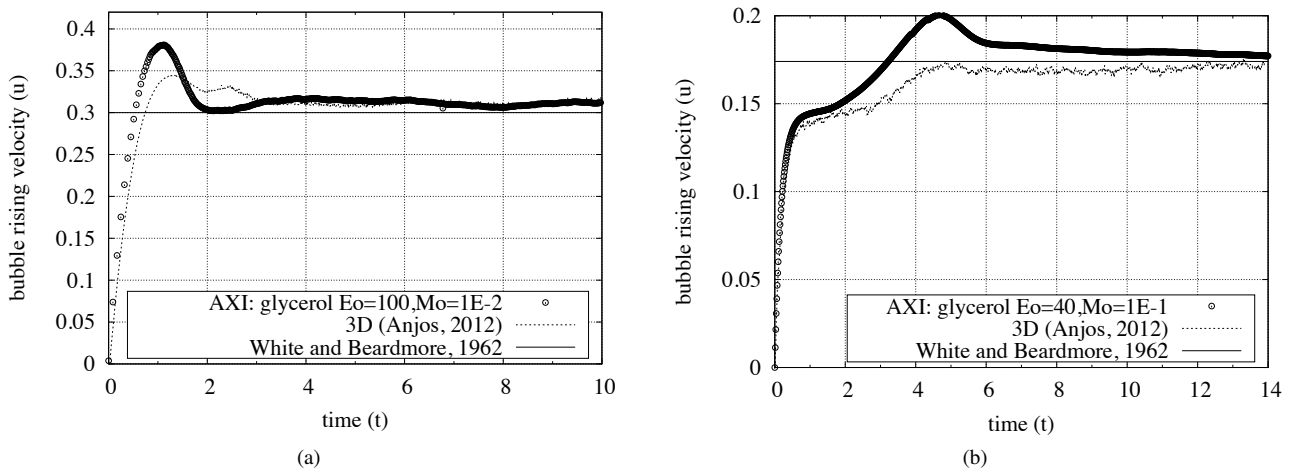
Figure 5: Rising of an air Taylor bubble immersed in a glycerol solution with dimensionless pair numbers set to (a) $Mo = 1e - 2$, $Eo = 100$ and (b) $Mo = 1e - 1$, $Eo = 40$. The time evolution of the Bubble's center of mass velocity is compared to the terminal bubble's velocity found in White and Beardmore (1962). Velocity and time are non-dimensional.
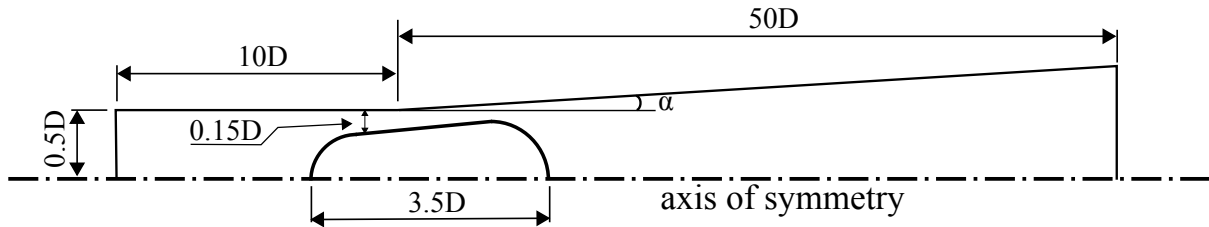

Figure 6: Axisymmetric numerical domain for the rising bubble in divergent channel. $D = 1$ stands for the non-dimensional diameter. $\alpha = 2^o$ is the angle of divergence found in the experiments.

important noting that an extra mesh refinement level is required to solve the liquid film formed between the wall and the confined bubble, thus the total number of mesh elements increases dramatically.

In Fig. (7) shows the evolution of the air bubble aspect ratio, $\chi = b_l/b_w$, as a function of the axial position, L_d, for two solutions namely DW and HMDSO, from the diverging section, where b_l stands for the bubble length and b_w for the bubble width. The comparison between numerical with experimental data has been made. Additionally a least-square fitting has been applied to the experimental data. Good agreement has been found for the initial diverging section for both figures, however the numerical simulation of HMDSO solution presented aspect ratio oscillation for $L_d > 70$. Both solutions presented very low Eo number (< 3), which makes the interfacial dynamics faster and the consequently appearence of interfacial waves. For the DW solution, the non-dimensional paramenters were set to $Eo = 0.59$, $N = 95757$ and $Mo = 2.27e - 11$, and for the HMDSO solution $Eo = 2.41$, $N = 227214$ and $Mo = 2.74e - 10$ were set. Both simulations used 6 days of computational resources in a shared memory machine using openMP (OpenMP Architecture Review Board (2008)) as parallelization tool.

A comparison between numerical and experimental results for DW+G in the 4° divergent pipe is presented in Fig. (8) for the evolution of the bubble aspect ratio, $\chi = b_l/b_w$ and the air bubble rising velocity for DW+G. We note good agreement with experiments and the least-square fitting plotted in the same figure. Moreover, the simulation was able to capture the velocity variation with time for the simulation. It was noted an initial increase of velocity in the first section of the pipe. This is due to action of the gravity field on the initial bubble condition. Later, the bubble is desacelerated till $u = 0.2$ and acelerated when passing through the diverging section.

Figure (9) shows the shape progression with time of an elongated air bubble immersed in the DW+G solution for five snapshots. The dimensionless numbers were set to $Eo = 0.73$, $N = 1506$ and $Mo = 1.74e - 7$. As can be seen, the initial condition presents interfacial waves which are propagated backwards from $t = 2.94$ to $t = 5.64$ where the transition from constant to variable cross-section is placed. After $t \approx 8$ the bubble decreases it aspect ration χ and a spherical cap bubble takes place.

We have not seen any topological changing in the interface at all simulations presented here, therefore no bubble break-up has occurred. For all simulations presented here, the same mesh condition conditions were used, i.e. the domain discretization used approximately 34000 nodes and 22000 triangle elements. The interface mesh (boundary and bubble) had approximately 2500 nodes and 2500 line segments.

	ρ	μ	ν	γ	$\mathcal{V}$
	$\left(\text{g/cm}^3\right)$	(mPa.s)	$\left(\text{mm}^2/\text{s}\right)$	(mN/m)	$\left(\text{mm}^3 \text{ or } \mu l\right)$
DW	1	1	1	75.6	$35.1 < \mathcal{V} < 35.5$
DW+G	1.128	9.01	7.988	69	$35.0 < \mathcal{V} < 40.0$
SO	0.97	970	1000	21.2	$26.5 < \mathcal{V} < 58.6$
HMDSO	0.824	0.536	0.65	15.3	$56.5 < \mathcal{V} < 60.0$

Table 2: Physical properties of the different liquids and bubble volume, $\mathcal{V}$, explored in the experiments. All the experiments were conducted at 25°C. DW stands for degassed water, G stands for glycerol and SO stands for silicone oil.
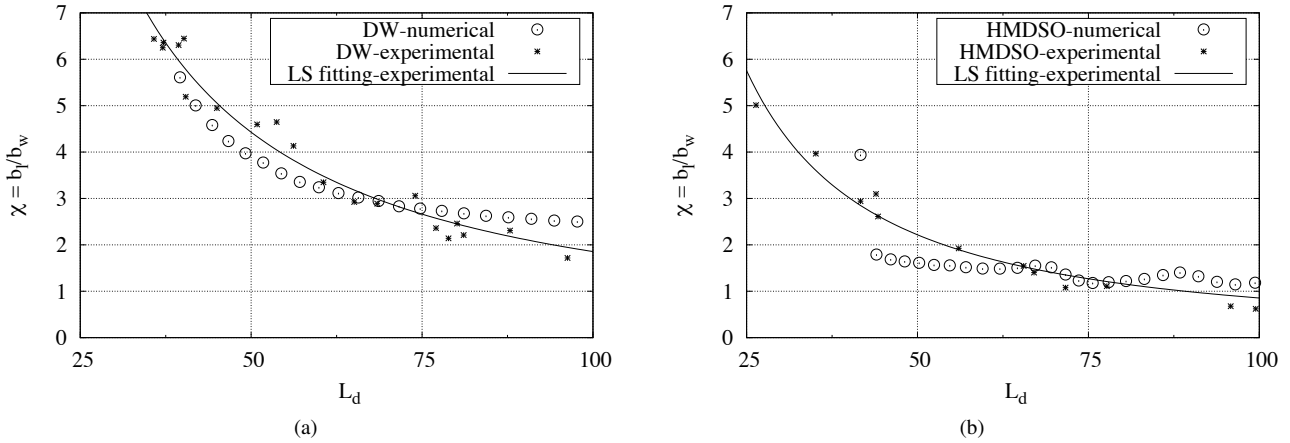

Figure 7: Comparison between numerical and experimental results for two solutions in the 4° divergent pipe. Evolution of the bubble aspect ratio, $\chi = b_l/b_w$, as a function of the axial position, L_d. (a) DW solution and (b) HMDSO solution.
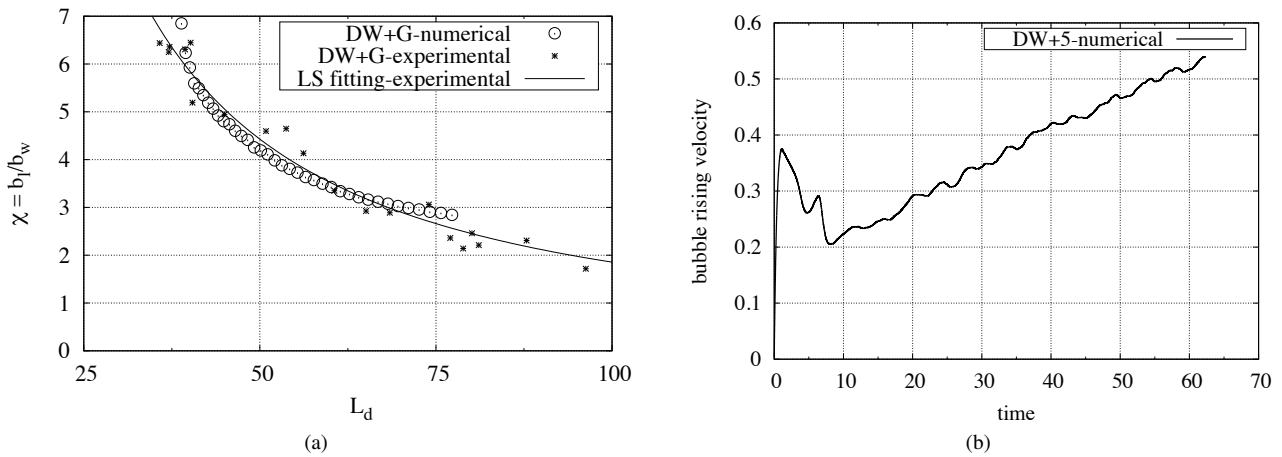

Figure 8: (a) Comparison between numerical and experimental results for DW+G in the 4° divergent pipe. Evolution of the bubble aspect ratio, $\chi = b_l/b_w$, as a function of the axial position, L_d and (b) air bubble rising velocity for DW+G solution. Velocity and time are non-dimensional.

5. CONCLUSIONS

We presented a study about the dynamics of a rising bubble in a vertical divergent pipe. Our experiments revealed the effect of viscosity, gravity and surface tension on the dynamics of a rising bubble. Numerical simulations using axisymmetric equations of two-phase flow motion has been performed to evaluate the bubble shape and the transition between elongated and spherical cap bubbles. We have found good agreement for the evolution of the bubble aspect ratio between numerical and experimental data for solutions tested in this work. It is worth noting that the initial conditions found in the experiments are extreamly difficult to be reproduced by the numerical simulation, therefore results can slightly differ. An extension of this work will be focused on the study the effect of oscillations and perturbations on the path of the
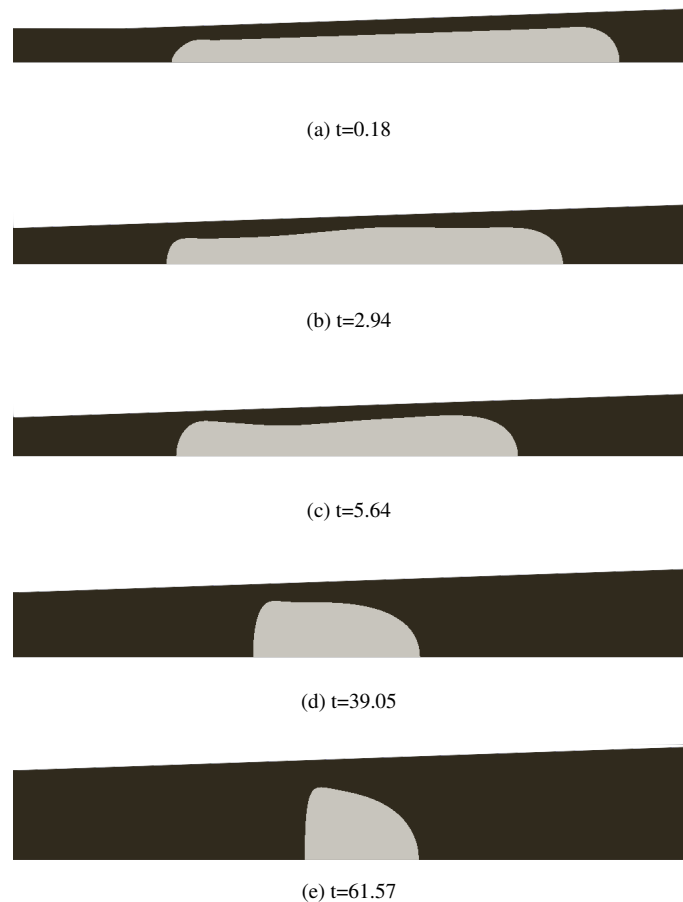
(a) t=0.18

(b) t=2.94

(c) t=5.64

(d) t=39.05

(e) t=61.57

Figure 9: Axisymmetric numerical results for rising bubble in divergent channel for $Eo = 2.44$, $Mo = 6.46e-6$. Images of bubble at different positions along the tube, where gravity is from right to left and. Time is dimensionless. (a) initial condition $t = 0.18$, (b)-(d) bubble shape evolution with time 2.94, 5.64, 39.05 and 61.57 respectively.

bubble. In near future, we will consider liquid flow in a convergent-divergent tube together with the presence of a bubble. In this case, break-up or fragmentation of the bubble can easily occur and this can used as an efficient micro-bubble generator (e.g. see Okamoto *et al.* (2007)).

6. ACKNOWLEDGEMENTS

7. REFERENCES

Anjos, G., 2012. *A 3D ALE Finite Element Method for Two-Phase Flows with Phase Change*. Ph.D. thesis, École Polytechnique Fédérale de Lausanne.

Anjos, G., Borhani, N., Mangiavacchi, N. and Thome, J., 2014. "3d moving mesh finite element method for two-phase flows". *Journal of Computational Physics*, Vol. 270, pp. 366–377. doi:10.1016/j.jcp.2014.03.067.

Assillous, P. and Quéré, D., 2002. "Bubbles creeping in a viscous liquid along a slightly inclined plane". *Europhysics Letters*, Vol. 59, pp. 370–376.

Balay, S., Brown, J., Buschelman, K., Eijkhout, V., Gropp, W., Kaushik, D., Knepley, M., McInnes, L., Smith, B. and Zhang, H., 2011a. "PETSc users manual". Technical Report ANL-95/11 - Revision 3.2, Argonne National Laboratory.

Balay, S., Brown, J., Buschelman, K., Gropp, W., Kaushik, D., Knepley, M., McInnes, L., Smith, B. and Zhang, H., 2011b. "PETSc Web page,". Http://www.mcs.anl.gov/petsc.

Batchelor, G.K., 1987. "The stability of a large gas bubble rising through liquid". *J. Fluid Mech.*, Vol. 184, pp. 399–422.

Bonometti, T. and Magnaudet, J., 2006. "Transition from spherical cap to toroidal bubbles". *Physics of Fluids*, Vol. 18,

p. 052102.

Brackbill, J. and Kothe, D., 1992. "A continuum method for modeling surface tension". *Journal of Computational Physics*, Vol. 100, pp. 335–354.

Bretherton, F.P., 1961. "The motion of long bubbles in tubes". *J. Fluid Mech.*, Vol. 19, pp. 166–168.

Brown, R., 1965. "The mechanism of large bubbles intubes. i. bubbles velocities in stagnant liquids". *Canadian Journal of Chemical Engineering*, Vol. 43, pp. 217–223.

Bugg, J., Mack, K. and Rezkallah, K.S., 1998. "A numerical model of taylor bubbles rising through stagnant liquids in vertical tubes". *International Journal of Multiphase Flow*, Vol. 24, pp. 271–281.

Clanet, C., Hérauld, P. and Searby, G., 2004. "On the motion of bubbles in vertical tubes of arbitrary cross-sections: some complements to the dimitrescu-taylor problem". *J. Fluid Mech.*, Vol. 519, pp. 359–376.

Clift, R., Grace, J.R. and Weber, M.E., 1978. *Bubbles, drops and particles*. Academic Press.

Davies, R.M. and Taylor, G., 1950. "The mechanics of large bubbles rising through extended liquids and through liquids in tubes". *Proceedings of the Royal Society A*, Vol. 200, pp. 375–390.

de Gennes, P.G., Brochard-Wyart, F. and Quéré, D., 2002. *Gouttes, bulles, perles et ondes*. Éditions Belin.

de Lózar, A., Hazel, A.L. and Juel, A., 2007. "Scaling properties of coating flows in rectangular channels". *Phys. Rev. Lett.*, Vol. 99, No. 234501.

Duclaux, V., Clanet, C. and Quéré, D., 2006. "The effects of gravity on the capillary instability in tubes". *Journal of Fluid Mechanics*, Vol. 556, pp. 217–226.

Funada, T., Joseph, D.D., Maehara, T. and Yamashita, S., 2005. "Ellipsoidal model of the rise of a taylor bubble in a round tube". *Int. J. Multiphase Flow*, Vol. 31, pp. 473–491.

Hirt, C. and Nichols, B., 1981. "Volume of fluid (vof) method for the dynamics of free boundaries". *Journal of Computational Physics*, Vol. 39, pp. 201–225.

Levine, H. and Yang, Y., 1990. "A rising bubble in a tube". *Phys. Fluids*, Vol. 2(4), pp. 542–546.

Lu, X. and Prosperetti, A., 2006. "Axial stability of taylor bubbles". *J. Fluid Mech.*, Vol. 568, pp. 173–192.

Muradoglu, M. and Stone, H.A., 2007. "Motion of large bubbles in curved channels". *J. Fluid Mech.*, Vol. 570, pp. 455–466.

Okamoto, K., Hashiguchi, K., Peixinho, J., Fujiwara, A., Takagi, S. and Matsumoto, Y., 2007. "Breakup of a bubble into a convergent-divergent flow". In *Proceedings of the 6th International Conference on Multiphase Flow*.

OpenMP Architecture Review Board, 2008. "OpenMP application program interface version 3.0". URL http://www.openmp.org/mp-documents/spec30.pdf.

Shewchuk, J.R., 1997. *Delaunay Refinement Mesh Generation*. Ph.D. thesis, School of Computer Science, Pittsburg, USA.

Viana, F., Pardo, R., Yánez, R., Trallero, J.L. and Joseph, D.D., 2003. "Universal correlation for the rise velocity of long gas bubbles in round pipes". *J. Fluid Mech.*, Vol. 494, pp. 379–398.

Wegener, P.P. and Parlange, J.Y., 1973. "Spherical cap bubbles". *Annual Review of Fluid Mechanics*, Vol. 5, pp. 79–100.

White, E. and Beardmore, R., 1962. "The velocity of rise of single cylindrical air bubbles through liquids contained in vertical tubes". *Chemical Engineering Science*, Vol. 17, pp. 351–361.

Zukoski, E.E., 1966. "Influence of viscosity, surface tension, and inclination angle on motion of long bubbles in closed tubes". *J. Fluid Mech.*, Vol. 25, pp. 821–837.